

Picocavity-Enhanced Raman Spectroscopy of Physisorbed H₂ and D₂ Molecules

Akitoshi Shiotari,^{1,*} Shuyi Liu,^{1,†} George Trenins,² Toshiki Sugimoto,^{3,4} Martin Wolf,¹ Mariana Rossi,^{2,‡} and Takashi Kumagai^{3,4,§}

¹*Department of Physical Chemistry,
Fritz-Haber Institute of the Max-Planck Society,
Faradayweg 4-6, 14195 Berlin, Germany*

²*Max-Planck-Institute for Structure and Dynamics of Matter, 22761 Hamburg, Germany*

³*Institute for Molecular Science, National Institutes
of Natural Sciences, 444-8585 Okazaki, Japan*

⁴*The Graduate University for Advanced Studies,
SOKENDAI, 240-0193 Hayama, Japan*

(Dated: May 21, 2025)

Abstract

We report on tip-enhanced Raman spectroscopy of H_2 and D_2 molecules physisorbed within a plasmonic picocavity at 10 K. The intense Raman peaks resulting from the rotational and vibrational transitions are observed at subnanometer gap distances of the junction formed by an Ag tip and an Ag(111) surface, where a picocavity-enhanced field plays a crucial role. A significant redshift of the H-H stretch frequency is observed as the gap distance decreases, while the D-D stretch frequency is unaffected. Density functional theory, path-integral molecular dynamics, and quantum anharmonic vibrational energy calculations suggest that this unexpected isotope effect is explained by a different molecular density between H_2 and D_2 on the surface.

The adsorption of hydrogen molecules on solid surfaces is the first step in permeation for fuel storage [1], catalytic hydrogenation [2], hydrogen embrittlement [3], and nuclear-spin isomer conversion [4]. To understand and control the elementary processes in such physical and chemical phenomena, hydrogen adsorption has been intensively studied in surface science [5–7]. Specifically, hydrogen, the lightest molecule, exhibits unique quantum effects that differ from those of other molecules when it is physisorbed on a surface through van der Waals interactions [8–17]. However, only a few methods are available for characterizing such physisorption systems as the weak adsorption energy (< 100 meV) necessitates measurements at cryogenic temperatures. Low-temperature scanning tunneling microscopy has been employed as a local characterization technique to investigate the dynamics of hydrogen molecules weakly adsorbed on surfaces [18–28]. Several studies have observed characteristic features in conductance spectra, attributed to the rotational transition of molecular hydrogen in the scanning tunneling microscopy (STM) junction [21–24]. However, the interpretation remains controversial; the features within the corresponding energy range [30–60 meV ($\sim 240\text{--}480$ cm^{-1}) for H_2] could be attributed to configuration switching [18, 29, 30], to a molecule–substrate stretching mode [31], or to multiple phonon excitation [32]. Additionally, the stretching mode has never been observed in these studies.

Raman spectroscopy is a promising technique for characterizing hydrogen molecules on surfaces, as it allows the observation of both rotational and vibrational transitions of homonuclear diatomic molecules. Although the detection demands exceptional sensitivity due to the intrinsically small cross section, single-molecule detection can be achieved by tip-enhanced Raman spectroscopy (TERS) and surface-enhanced Raman spectroscopy (SERS)

[33–37]. Recent studies have established that picocavities, atomic-scale protrusions present in plasmonic nanojunctions, play a crucial role in achieving extreme confinement of the electromagnetic field to angstrom scales [37–39], resulting in a significant enhancement of Raman scattering [40–42] and ultrahigh spatial resolution [43–46]. Yet, the exceptional sensitivity in TERS and SERS has been demonstrated primarily for organic molecules chemisorbed onto the substrate, where the enhancement benefits from chemical effects arising from the molecule–surface (and molecule–tip) interactions [47]. Therefore, applying TERS and SERS to physisorbed systems has remained challenging.

Here, we demonstrate that low-temperature TERS (LT-TERS) can detect hydrogen molecules physisorbed onto an Ag(111) surface with an Ag tip [Fig. 1(a), inset], allowing for the identification of their rotational and vibrational states. Furthermore, precise gap-distance control enables us to investigate not only the contribution of the picocavity field to the Raman scattering process but also the influence of tip proximity on the rotational and vibrational energies of the molecules through nontrivial nuclear quantum effects. Density functional theory (DFT), path-integral molecular dynamics, and quantum vibrational energy calculations suggest that the tip–molecule–surface potential energy profiles are critically affected by the intermolecular and tip–molecular interactions, leading to unusual isotope effects on vibrational frequencies.

The LT-TERS experiments were performed in an ultrahigh vacuum chamber [see Sec. I-A of Supplemental Material (SM) [48]]. The 532-nm incident laser beam was linearly polarized along the tip axis and focused on the apex of a focused-ion-beam-sharpened Ag tip [40, 42] using an *in situ* parabolic mirror, and the scattering light was detected by an *ex situ* spectrometer. We conducted DFT calculations [50, 51] of H_2/D_2 on a 4×4 Ag(111) (periodic) surface, employing the Perdew-Burke-Ernzerhof exchange-correlation functional and screened pairwise van der Waals interactions [52] (see SM Sec. I-B [48]). The preferred adsorption sites (fcc or hcp hollow) and binding energies (~ 30 meV) were in very good agreement with previous studies of isolated molecules on the surface [55, 65]. Unless specified otherwise, we considered a coverage of 0.69 monolayer (ML), motivated by the results of path-integral molecular dynamics simulations at low temperature (see SM Sec. I-B [48]). At 0.69 ML coverage, the intermolecular attractive interaction increases the binding energy by 55 meV compared to the lowest coverage of 0.06 ML considered here (Fig. S3). Over the sample, we placed the Ag-tip model shown in SM Sec. I-B [48] (see also Fig. S4), which was

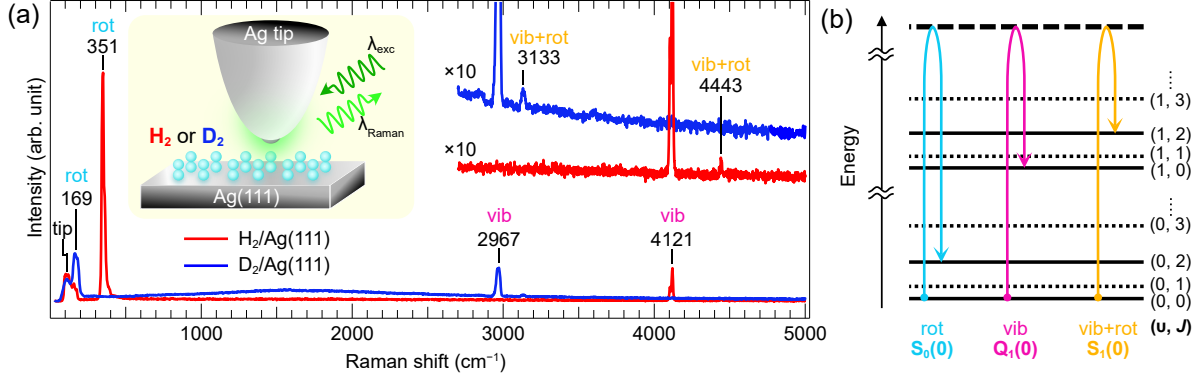


FIG. 1. (a) TERS spectra of H_2 (red) and D_2 (blue) on $\text{Ag}(111)$ with a Ag tip at 10 K (sample bias voltage $V_s = 10$ mV, tunneling current $I_t = 1.0$ nA). The left inset shows a schematic of the experiment. λ_{exc} and λ_{Raman} denote the wavelength of the incident laser and Raman scattering, respectively. The right inset shows magnified spectra in the high wavenumber regions. The peak originating from tip phonon modes is denoted as “tip.” (b) Energy diagram of the vibrational and rotational levels of an H_2 or D_2 molecule. The solid lines represent the levels for *para*- H_2 and *ortho*- D_2 , while the dotted lines are those for *ortho*- H_2 and *para*- D_2 . The dashed bold line represents a virtual state. The arrows indicate Raman-active transitions referred to as “rot,” “vib,” and “rot+vib.” v and J denote the vibrational and rotational quantum numbers, respectively.

also previously discussed in Refs. [41, 46, 54].

H_2 or D_2 gas was introduced into the chamber where a clean $\text{Ag}(111)$ surface was cooled at 10 K (see SM Sec. I-A [48]). Regardless of laser illumination, no static hydrogen molecules on the surface were imaged with STM (Fig. S1). In contrast, clear peaks were observed in TERS spectra under these conditions. Figure 1(a) displays typical TERS spectra of H_2 and D_2 on $\text{Ag}(111)$. For H_2 , intense peaks were observed at 351 and 4121 cm^{-1} , along with a weak peak at 4443 cm^{-1} . Similarly, for D_2 , intense peaks appeared at 169 and 2967 cm^{-1} , with a weak peak at 3133 cm^{-1} . The three peaks can be assigned to rotational and vibrotational modes of hydrogen. Note that broad or asymmetric peak shapes are artifacts in the wide wavenumber range spectra (see SM Sec. I-A [48]). The feature around 100 cm^{-1} common to both spectra originates from phonon modes of the Ag tip [41, 66], which is present even in the absence of hydrogen adsorption (Fig. S2). Figure 1(b) depicts the energy diagram of rotational and vibrational levels and allowed transitions under the Raman selection rule. The observed peaks, in order from lowest to highest, correspond to the lowest-energy rotational transition

[$S_0(0)$; “rot” labeled in Fig. 1(a)], the lowest-energy vibrational transition [$Q_1(0)$; “vib”], and their combination [$S_1(0)$; “rot+vib”], respectively. The three modes were also observed in high-resolution electron energy loss spectroscopy of hydrogen on a polycrystalline Ag film [8] and a Cu(001) surface [9] at approximately 10–12 K; however, better energy resolution ($<10\text{ cm}^{-1}$) in TERS than that of the electron energy loss spectroscopy ($>28\text{ cm}^{-1}$ [9]) makes the redshifts from gas-phase hydrogen more discernible (Table S4). We should also note that only the stable nuclear-spin isomer of each isotope, i.e., *para*-H₂ and *ortho*-D₂ [Fig. 1(b)], is detected in TERS (Fig. S2). On the surface, the stable isomer is dominant due to the *ortho*–*para* conversion [4, 8, 55] (see SM Sec. II-A [48]).

The rotational transition at 351 cm^{-1} for H₂/Ag(111) [Fig. 1(a)] is slightly redshifted from 354 cm^{-1} in the gas phase [62]. We calculate the H-H bond length to be 75.4 pm on Ag(111) (cf. 75.1 pm in the gas phase). Considering a rigid-rotor approximation, the rotational transition energy of *para*-H₂ is calculated to be 353 cm^{-1} on the surface, compared to 356 cm^{-1} in the gas phase, showing good agreement with the experiment. Notably, the H-H bonding distance of H₂ on Ag(111) varied by only 0.06 pm at the closest tip position with respect to simulations without any tip. This suggests that the hydrogen molecules on the surface and in the STM junction behave as nearly free rotors.

In the TERS spectrum [Fig. 1(a)], the vibrational frequency of 4121 cm^{-1} exhibits a redshift relative to the gas-phase value of 4161 cm^{-1} [62]. The vibrational transition energy is calculated to be 4088 cm^{-1} on the surface (without the Ag tip), after applying a scale factor to the calculations performed in the harmonic approximation (see SM Sec. I-C [48]; see also Fig. S8 for a simulated LT-TERS spectrum [46]). The slight discrepancy between the experimental and calculated frequencies is consistent with the typical spurious softening of the Perdew-Burke-Ernzerhof functional. Compared to the calculated gas-phase value, the vibrational frequency shows a redshift of $\sim 73\text{ cm}^{-1}$ upon the adsorption, which is larger than, but in reasonable agreement with the experiment.

The TERS intensity is strongly correlated with the localized surface plasmonic resonance (LSPR) of the tip–sample junction. In general, two types of enhancement mechanisms contribute to TERS [36, 47]: electromagnetic enhancement through LSPR and chemical enhancement originating from charge transfer between the target molecule and the tip or surface. In physisorption systems, the electromagnetic enhancement is expected to be dominant.

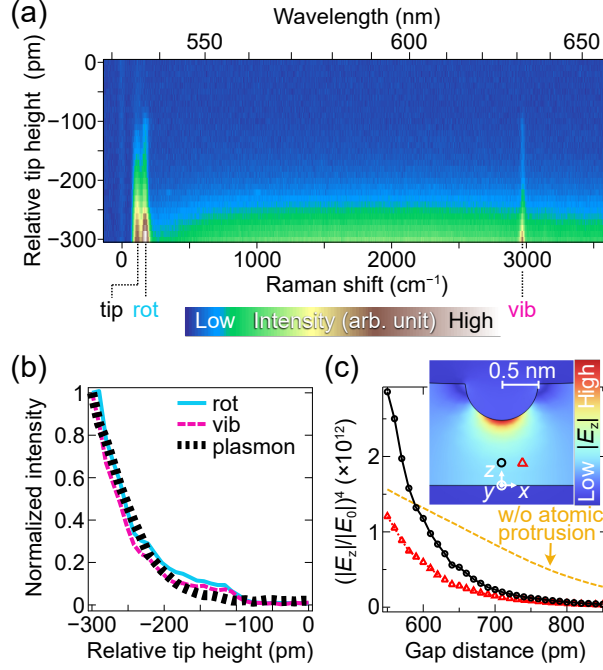


FIG. 2. (a) Waterfall plot for the TERS spectra during the tip approach to D₂/Ag(111). The origin of the vertical axis corresponds to a tip height 100 pm above the STM set point ($V_s = 10$ mV, $I_t = 0.1$ nA). (b) Tip-height dependence of the Raman intensities, corresponding to the vertical line profiles of “rot,” “vib,” and the plasmonic background (2000 cm⁻¹). The intensity is normalized for each profile. (c) Gap-distance dependence of the field enhancement factor simulated by the finite element method. The STM junction with a plasmonic picocavity is modeled using an Ag tip (30-nm radius of curvature) with an atomic-scale protrusion (0.5-nm radius) and a flat Ag sample plate (Fig. S9). The vertical electric field E_z at $\lambda_{\text{exc}} = 532$ nm is sampled and normalized with the incident field E_0 . The inset shows the $|E_z|$ distribution at a tip-sample gap distance of 0.9 nm. The black curve represents the field enhancement factor $(|E_z|/|E_0|)^4$ sampling at the location of the D₂ just below the tip (circle marker in the inset), while the red curve is that at the nearest neighboring D₂ (triangle). The orange curve shows the field enhancement at the same sampling point as the black curve but using an Ag tip without the atomic-scale protrusion.

To elucidate the role of electromagnetic enhancement, it is crucial to investigate the gap-distance dependence of TERS signals. Figure 2(a) shows the waterfall plot of the gap-distance-dependent TERS spectra recorded for D₂/Ag(111). When the tip approaches the surface, the TERS intensities of the rotational and vibrational modes increase apparently

exponentially [Fig. 2(b)], in agreement with the previously reported analytical model simplifying a plasmonic tip as a point dipole [60]. A broad background with a maximum at ~ 590 nm is attributed to electronic Raman scattering which reflects the spectral response of the LSPR in the junction [67]. The gap-distance-dependent intensities of both rotational and vibrational modes closely follow the plasmonic feature [Fig. 2(b)], indicating the dominant contribution of the gap-mode plasmon to the TERS enhancement. Additionally, we observed that changes in both the plasmon background and the molecular Raman peak occurred by an accidental modification of the tip-apex structure (Fig. S11), implying that the TERS enhancement is susceptible to the atomic-scale structure of the tip apex, which generates a plasmonic picocavity.

The gap-distance dependence of the TERS intensities is well reproduced by simulating the electronic field distribution in the Ag-tip–Ag-surface junction using the finite element method (see SM Sec. I-E [48]). To model the plasmonic picocavity, we assume an atomic-scale protrusion (0.5-nm radius of curvature) attached to a blunt tip body (Fig. S9). The black curve in Fig. 2(c) shows the field enhancement at the expected position of a D_2 molecule located beneath the Ag tip, indicating a steep increase as the tip approaches. We confirmed the critical role of this subnanometric structure in TERS; as shown by the orange curve in Fig. 2(c), the tip without the atomic-scale protrusion exhibits a more moderate increase of the field enhancement as the tip approaches, which does not reproduce the experimental data [Fig. 2(b)]. The red curve in Fig. 2(c) shows the field enhancement at a possible position of the nearest neighboring molecule [Fig. 2(c), inset], indicating much lower enhancement. Therefore, TERS can achieve “nearly” single-molecule sensitivity, even for physisorption systems. The contribution of LSPR to the TERS intensity was further confirmed by our excitation-wavelength dependent measurements (SM Sec. II-B [48]); a strong TERS peak was observed only when the scattering light wavelength matches with the resonance range of the LSPR (Fig. S10).

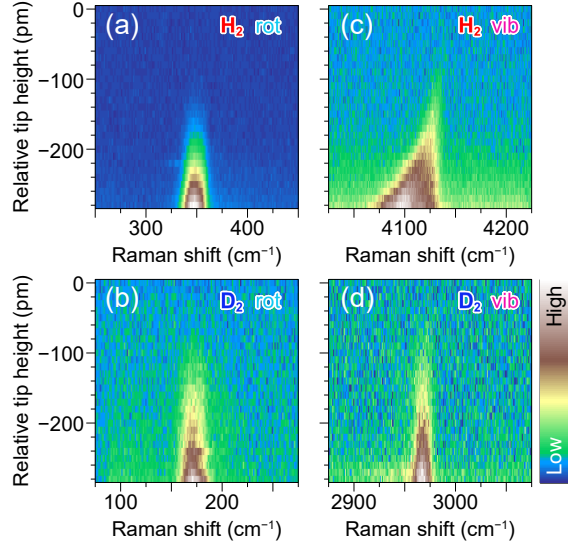


FIG. 3. (a–d) Waterfall plots of the high-resolution TERS spectra with different tip heights: (a) H_2 rot, (b) H_2 vib, (c) D_2 rot, and (d) D_2 vib. The origin of the tip height corresponds to a tip height 30 and 70 pm higher than the set point ($V_s = 10$ mV, $I_t = 0.1$ nA) for H_2 and D_2 , respectively.

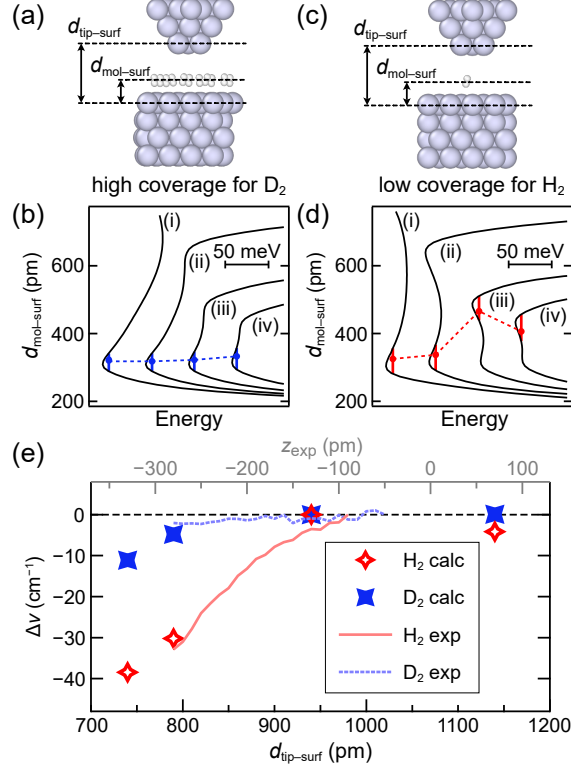


FIG. 4. (a) Simulated atomic structure of the junction at a tip-surface distance $d_{\text{tip-surf}}$ of 0.79 nm at a high coverage (0.69 ML). The light blue and white spheres represent Ag and H atoms, respectively. (b) Energy profiles along $d_{\text{mol-surf}}$ at the high coverage shown in (a). Curves (i)–(iv) indicate profiles obtained at $d_{\text{tip-surf}} = 1.14, 0.94, 0.79$, and 0.74 nm, respectively. For clarity, curves (ii)–(iv) are offset by 50, 100, and 150 meV, respectively, relative to (i) in the horizontal axis. The bullet on each potential indicates the average D₂ position, considering ZPE contributions (Table S3). The vertical lines indicates the ZPE levels and the dashed lines connecting the bullets serve only as a guide to the eye. (c) Same as (a) but at a lower coverage (0.06 ML). (d) Same as (b), but at the lower coverage shown in (c). The bullet on each potential indicates the average H₂ position, considering ZPE contributions (Table S2). (e) Shifts of the intramolecular stretch frequencies $\Delta\nu$ as a function of $d_{\text{tip-surf}}$. The empty red and filled blue bullets represent the calculated values of low-coverage H₂ and high-coverage D₂, respectively. The frequencies at $d_{\text{tip-surf}} = 0.94$ nm are used for the origin of the shifts. The solid red and dashed blue lines represent the experimental $\Delta\nu$ values for H₂ vib [Fig. 3(c)] and D₂ vib [(d)], respectively, as a function of the relative tip height z_{exp} (see SM Sec. II-C [48] for details). The minimum tip height, $z_{\text{exp}} = -280$ pm, is aligned with $d_{\text{tip-surf}} = 0.74$ nm.

TERS reveals the sensitivity of the rotational and vibrational states to the interactions between a target molecule and its local environment. Figures 3(a)–3(d) show the gap-distance dependence of high-resolution TERS spectra focusing on the rotational and vibrational modes of H_2 and D_2 . Notably, only the vibrational frequency of H_2 exhibits a significant redshift as the gap distance decreases [Fig. 3(c)]; H_2 shows a peak shift $\Delta\nu$ of -33 cm^{-1} with a 200 pm displacement of the tip, whereas $\Delta\nu$ is merely -2 cm^{-1} for D_2 . Additionally, the peak width of the H_2 vibrational mode also increases as the gap distance decreases (see SM Sec. II-C [48] for details). In contrast, the peak positions of the rotational modes for both H_2 [Fig. 3(a)] and D_2 [3(b)] are almost unchanged, consistent with our calculations showing that the interatomic distance is independent of the tip height, as described above.

The isotope dependence of the redshift of the vibrational band far exceeds the scale of typical isotope effects. To understand this anomalous behavior, we calculated the potential energy profile $V(d_{\text{mol-surf}}, d_{\text{tip-surf}})$ along the rigid vertical displacement of the center of mass of one molecule between the surface and the tip apex $d_{\text{mol-surf}}$ [Fig. 4(a)], while varying the tip-sample distance $d_{\text{tip-surf}}$ [see profiles (i)–(iv) at different $d_{\text{tip-surf}}$ in Fig. 4(b)]. At each $d_{\text{mol-surf}}$ position, we calculated the H_2 and D_2 harmonic intramolecular vibrational frequency ν_{harm} (see SM Sec. I-C [48]). The calculations indicate a pronounced coupling of the stretch coordinate r_{stretch} with the molecular translation along $d_{\text{mol-surf}}$, evidenced by a steep variation of ν_{harm} along this coordinate (Fig. S7). Furthermore, this variation changes depending on the tip-sample distance, leading us to define $\nu_{\text{harm}}(d_{\text{mol-surf}}, d_{\text{tip-surf}})$. As detailed in SM Sec. I-C [48], for each $d_{\text{tip-surf}}$, we constructed a model 2D Schrödinger equation in the coupled coordinates $d_{\text{mol-surf}}$ and r_{stretch} , parameterized by $V(d_{\text{mol-surf}}, d_{\text{tip-surf}})$ and $\nu_{\text{harm}}(d_{\text{mol-surf}}, d_{\text{tip-surf}})$. The solution of this model gives us the expected intramolecular stretch vibrational transition energy ν for each isotope, fully accounting for the anharmonic coupling between these coordinates. We concluded that if both H_2 and D_2 probe the same potential energy profile $V(d_{\text{mol-surf}}, d_{\text{tip-surf}})$ [Fig. 4(b)], for reasonable position-dependent stretch frequencies $\nu_{\text{harm}}(d_{\text{mol-surf}}, d_{\text{tip-surf}})$ the calculated peak shifts $\Delta\nu$ are in a ratio of at most 2:1 for $\text{H}_2\text{:D}_2$ (Tables S2 and S3), in disagreement with the measured 16:1 ratio (Fig. 3).

We demonstrate that this discrepancy can be resolved by accounting for density differences between H_2 and D_2 . At lower temperatures, the solids formed by H_2 and D_2 have

different molar volumes due to nuclear quantum effects [zero-point energy (ZPE) swelling [68]; see also SM Sec. I-B [48]]. As a result, solid D₂ is more than twice as dense as solid H₂ at 4.2 K [69]. Because the interaction potential between the molecules and the surface exhibits almost no corrugation [55], we expect that H₂ adsorbs on Ag(111) at 10 K more sparsely than D₂. To explore a limiting low-density regime, we repeated the calculations discussed in the previous paragraph for a coverage of 0.06 ML of H₂ [Fig. 4(c)]. As shown in Fig. 4(d), the reduced intermolecular interactions at the surface cause the minimum of $V(d_{\text{mol-surf}}, d_{\text{tip-surf}})$ along $d_{\text{mol-surf}}$ to lie closer to the tip instead of closer to the surface, as $d_{\text{tip-surf}}$ decreases [(i) to (iv)]. Consequently, the average position of the molecule center of mass [bullet points in Figs. 4(b) and (d)] also shifts toward the tip as $d_{\text{tip-surf}}$ decreases [dotted line in Fig. 4(d)]. Computing ν in this scenario with the 2D quantum model of $d_{\text{mol-surf}}$ and r_{stretch} , we find a larger variation with $d_{\text{tip-surf}}$ than in the higher-density case (Table S2). As shown in Fig. 4(e), considering the higher-density scenario for D₂ (the filled bullets) and the lower-density scenario for H₂ (the empty bullets) can account for the large isotope effect in the redshift of the stretch transition as the tip approaches. Figure 4(e) also shows the experimental $\Delta\nu$ values from the plots in Fig. 3 (the solid and dotted curves for H₂ and D₂, respectively; see also Fig. S12). Although the exact gap distance in STM experiment is hard to determine (see SM Sec. II-C [48]), the overlap of the experimental curves with the calculated plots in Fig. 4(e) shows good agreement. The remaining numerical discrepancies can be attributed to the limitation of the DFT level of theory (see SM Sec. I-B [48]), the exact tip-apex geometry, and to the uncertainty in determining the exact local surface coverage. Nevertheless, our results highlight the crucial role of intermolecular interactions in accurately interpreting vibrational spectroscopy of hydrogen isotopes in nanojunctions, where nuclear quantum effects have a significant impact [13].

In summary, with LT-TERS, we observed the rotational and vibrational transitions of local H₂ and D₂ molecules through the interaction with the picocavity field. Our results demonstrate that LT-TERS is applicable to weakly adsorbed molecules, offering deeper insights into the local structures, reactions, and dynamics of adsorbates, such as chemical reactivity at active sites [70] and surface diffusion (spillover) in catalytic processes [71], at the single-molecule level.

Acknowledgments—We thank Adnan Hammud for the Ag-tip fabrication. We thank Jun Yoshinobu and Heiko Appel for helpful discussions. T.S. acknowledges the support of JST

FOREST Grant No. JPMJFR221U. T.K. acknowledges the support of JST FOREST Grant No. JPMJFR201J.

* Corresponding author: shiotari@fhi-berlin.mpg.de

† Current address: Huazhong University of Science and Technology, Wuhan, China.

‡ Corresponding author: mariana.rossi@mpsd.mpg.de

§ Corresponding author: kuma@ims.ac.jp

- [1] N. W. Ockwig and T. M. Nenoff, Membranes for hydrogen separation, *Chem. Rev.* **107**, 4078 (2007).
- [2] L. Zhang, M. Zhou, A. Wang, and T. Zhang, Selective hydrogenation over supported metal catalysts: from nanoparticles to single atoms, *Chem. Rev.* **120**, 683 (2019).
- [3] X. Li, X. Ma, J. Zhang, E. Akiyama, Y. Wang, and X. Song, Review of hydrogen embrittlement in metals: hydrogen diffusion, hydrogen characterization, hydrogen embrittlement mechanism and prevention, *Acta Metallurgica Sinica* **33**, 759 (2020).
- [4] K. Fukutani and T. Sugimoto, Physisorption and ortho–para conversion of molecular hydrogen on solid surfaces, *Prog. Surf. Sci* **88**, 279 (2013).
- [5] K. Christmann, Interaction of hydrogen with solid surfaces, *Surf. Sci. Rep.* **9**, 1 (1988).
- [6] G. Vidali, G. Ihm, H.-Y. Kim, and M. W. Cole, Potentials of physical adsorption, *Surf. Sci. Rep.* **12**, 135 (1991).
- [7] L. W. Bruch, R. D. Diehl, and J. A. Venables, Progress in the measurement and modeling of physisorbed layers, *Rev. Mod. Phys.* **79**, 1381 (2007).
- [8] P. Avouris, D. Schmeisser, and J. E. Demuth, Observation of rotational excitations of H₂ adsorbed on Ag surfaces, *Phys. Rev. Lett.* **48**, 199 (1982).
- [9] S. Andersson and J. Harris, Observation of rotational transitions for H₂, D₂, and HD adsorbed on Cu(100), *Phys. Rev. Lett.* **48**, 545 (1982).
- [10] C. F. Yu, K. B. Whaley, C. S. Hogg, and S. J. Sibener, Selective adsorption resonances in the scattering of *n*-H₂, *p*-H₂, *n*-D₂ and *o*-D₂ from Ag(111), *Phys. Rev. Lett.* **51**, 2210 (1983).
- [11] M. Sakurai, T. Okano, and Y. Tuzi, Ortho-para conversion of *n*-H₂ physisorbed on Ag(111) near two-dimensional condensation conditions, *Appl. Surf. Sci.* **33**, 245 (1988).
- [12] G. Anger, A. Winkler, and K. Rendulic, Adsorption and desorption kinetics in the systems

- $\text{H}_2/\text{Cu}(111)$, $\text{H}_2/\text{Cu}(110)$ and $\text{H}_2/\text{Cu}(100)$, *Surf. Sci.* **220**, 1 (1989).
- [13] K. A. Williams, B. K. Pradhan, P. C. Eklund, M. K. Kostov, and M. W. Cole, Raman spectroscopic investigation of H_2 , HD, and D_2 physisorption on ropes of single-walled, carbon nanotubes, *Phys. Rev. Lett.* **88**, 165502 (2002).
 - [14] K. Fukutani, K. Yoshida, M. Wilde, W. A. Diño, M. Matsumoto, and T. Okano, Photostimulated desorption and ortho-para conversion of H_2 on Ag surfaces, *Phys. Rev. Lett.* **90**, 096103 (2003).
 - [15] K. Niki, T. Kawauchi, M. Matsumoto, K. Fukutani, and T. Okano, Mechanism of the ortho-para conversion of hydrogen on Ag surfaces, *Phys. Rev. B* **77**, 201404(R) (2008).
 - [16] T. Sugimoto and K. Fukutani, Effects of rotational-symmetry breaking on physisorption of ortho-and para- H_2 on Ag(111), *Phys. Rev. Lett.* **112**, 146101 (2014).
 - [17] T. Sugimoto, Y. Kunisada, and K. Fukutani, Inelastic electron tunneling mediated by a molecular quantum rotator, *Phys. Rev. B* **96**, 241409(R) (2017).
 - [18] J. A. Gupta, C. P. Lutz, A. J. Heinrich, and D. M. Eigler, Strongly coverage-dependent excitations of adsorbed molecular hydrogen, *Phys. Rev. B* **71**, 115416 (2005).
 - [19] R. Temirov, S. Soubatch, O. Neucheva, A. C. Lassise, and F. S. Tautz, A novel method achieving ultra-high geometrical resolution in scanning tunnelling microscopy, *New J. Phys.* **10**, 053012 (2008).
 - [20] C. Lotze, M. Corso, K. J. Franke, F. von Oppen, and J. I. Pascual, Driving a macroscopic oscillator with the stochastic motion of a hydrogen molecule, *Science* **338**, 779 (2012).
 - [21] S. Li, A. Yu, F. Toledo, Z. Han, H. Wang, H. He, R. Wu, and W. Ho, Rotational and vibrational excitations of a hydrogen molecule trapped within a nanocavity of tunable dimension, *Phys. Rev. Lett.* **111**, 146102 (2013).
 - [22] F. D. Natterer, F. Patthey, and H. Brune, Distinction of nuclear spin states with the scanning tunneling microscope, *Phys. Rev. Lett.* **111**, 175303 (2013).
 - [23] F. D. Natterer, F. Patthey, and H. Brune, Resonant-enhanced spectroscopy of molecular rotations with a scanning tunneling microscope, *ACS Nano* **8**, 7099 (2014).
 - [24] A. J. Therrien, A. Pronschinske, C. Murphy, E. A. Lewis, M. L. Liriano, M. D. Marcinkowski, and E. C. H. Sykes, Collective effects in physisorbed molecular hydrogen on Ni/Au(111), *Phys. Rev. B* **92**, 161407(R) (2015).
 - [25] S. Liu, A. Shiotari, D. Baugh, M. Wolf, and T. Kumagai, Enhanced resolution imaging of

- ultrathin ZnO layers on Ag(111) by multiple hydrogen molecules in a scanning tunneling microscope junction, *Phys. Rev. B* **97**, 195417 (2018).
- [26] P. Merino, A. Rosławska, C. C. Leon, A. Grewal, C. Große, C. González, K. Kuhnke, and K. Kern, A single hydrogen molecule as an intensity chopper in an electrically driven plasmonic nanocavity, *Nano Lett.* **19**, 235 (2018).
- [27] L. Wang, Y. Xia, and W. Ho, Atomic-scale quantum sensing based on the ultrafast coherence of an H₂ molecule in an STM cavity, *Science* **376**, 401 (2022).
- [28] L. Wang, D. Bai, Y. Xia, and W. Ho, Electrical manipulation of quantum coherence in a two-level molecular system, *Phys. Rev. Lett.* **130**, 096201 (2023).
- [29] W. H. A. Thijssen, D. Djukic, A. F. Otte, R. H. Bremmer, and J. M. van Ruitenbeek, Vibrationally induced two-level systems in single-molecule junctions, *Phys. Rev. Lett.* **97**, 226806 (2006).
- [30] A. Halbritter, P. Makk, S. Csonka, and G. Mihály, Huge negative differential conductance in Au–H₂ molecular nanojunctions, *Phys. Rev. B* **77**, 075402 (2008).
- [31] Y. Li, S. Kaneko, S. Fujii, and M. Kiguchi, Symmetry of single hydrogen molecular junction with Au, Ag, and Cu electrodes, *J. Phys. Chem. C* **119**, 19143 (2015).
- [32] M. L. Trouwborst, E. H. Huisman, S. J. van der Molen, and B. J. van Wees, Bistable hysteresis and resistance switching in hydrogen-gold junctions, *Phys. Rev. B* **80**, 081407(R) (2009).
- [33] G. Haran, Single-molecule Raman spectroscopy: a probe of surface dynamics and plasmonic fields, *Acc. Chem. Res.* **43**, 1135 (2010).
- [34] S.-Y. Ding, J. Yi, J.-F. Li, B. Ren, D.-Y. Wu, R. Panneerselvam, and Z.-Q. Tian, Nanostructure-based plasmon-enhanced Raman spectroscopy for surface analysis of materials, *Nat. Rev. Mater.* **1**, 16021 (2016).
- [35] X. Wang, S.-C. Huang, S. Hu, S. Yan, and B. Ren, Fundamental understanding and applications of plasmon-enhanced Raman spectroscopy, *Nat. Rev. Phys.* **2**, 253 (2020).
- [36] T. I. Itoh, M. Procházka, Z.-C. Dong, W. Ji, Y. S. Yamamoto, Y. Zhang, and Y. Ozaki, Toward a new era of SERS and TERS at the nanometer scale: From fundamentals to innovative applications, *Chem. Rev.* **123**, 1552 (2023).
- [37] C. Höppener, J. Aizpurua, H. Chen, S. Gräfe, A. Jorio, S. Kupfer, Z. Zhang, and V. Deckert, Tip-enhanced Raman scattering, *Nat. Rev. Methods Primers* **4**, 47 (2024).
- [38] F. Benz, M. K. Schmidt, A. Dreismann, R. Chikkaraddy, Y. Zhang, A. Demetriadou,

- C. Carnegie, H. Ohadi, B. De Nijs, R. Esteban, J. Aizpurua, and J. J. Baumberg, Single-molecule optomechanics in “picocavities”, *Science* **354**, 726 (2016).
- [39] M. Urbietta, M. Barbry, Y. Zhang, P. Koval, D. Sánchez-Portal, N. Zabala, and J. Aizpurua, Atomic-scale lightning rod effect in plasmonic picocavities: A classical view to a quantum effect, *ACS Nano* **12**, 585 (2018).
- [40] S. Liu, M. Müller, Y. Sun, I. Hamada, A. Hammud, M. Wolf, and T. Kumagai, Resolving the correlation between tip-enhanced resonance raman scattering and local electronic states with 1 nm resolution, *Nano Lett.* **19**, 5725 (2019).
- [41] S. Liu, F. P. Bonafe, H. Appel, A. Rubio, M. Wolf, and T. Kumagai, Inelastic light scattering in the vicinity of a single-atom quantum point contact in a plasmonic picocavity, *ACS Nano* **17**, 10172 (2023).
- [42] Y. Park, I. Hamada, A. Hammud, T. Kumagai, M. Wolf, and A. Shiotari, Atomic-precision control of plasmon-induced single-molecule switching in a metal–semiconductor nanojunction, *Nat. Commun.* **15**, 6709 (2024).
- [43] R. Zhang, Y. Zhang, Z. Dong, S. Jiang, C. Zhang, L. Chen, L. Zhang, Y. Liao, J. Aizpurua, Y. Luo, J. L. Yang, and J. G. Hou, Chemical mapping of a single molecule by plasmon-enhanced Raman scattering, *Nature* **498**, 82 (2013).
- [44] J. Lee, K. T. Crampton, N. Tallarida, and V. A. Apkarian, Visualizing vibrational normal modes of a single molecule with atomically confined light, *Nature* **568**, 78 (2019).
- [45] J. Xu, X. Zhu, S. Tan, Y. Zhang, B. Li, Y. Tian, H. Shan, X. Cui, A. Zhao, Z. Dong, J. Yang, Y. Luo, B. Wang, and J. G. Hou, Determining structural and chemical heterogeneities of surface species at the single-bond limit, *Science* **371**, 818 (2021).
- [46] Y. Litman, F. P. Bonafé, A. Akkoush, H. Appel, and M. Rossi, First-principles simulations of tip enhanced Raman scattering reveal active role of substrate on high-resolution images, *J. Phys. Chem. Lett.* **14**, 6850 (2023).
- [47] R. Chen and L. Jensen, Interpreting chemical enhancements of surface-enhanced Raman scattering, *Chem. Phys. Rev.* **4** (2023).
- [48] See Supplemental Material for detailed experimental and theoretical methods, additional figures, and tables, which includes Refs. [4, 8, 9, 11, 14, 15, 17, 18, 40, 41, 46, 49–64].
- [49] R. L. Summers, Empirical observations on the sensitivity of hot cathode ionization type vacuum gages, NASA Technical Report **NASA-TN-D-5285** (1969).

- [50] V. Blum, R. Gehrke, F. Hanke, P. Havu, V. Havu, X. Ren, K. Reuter, and M. Scheffler, Ab initio molecular simulations with numeric atom-centered orbitals, *Comput. Phys. Commun.* **180**, 2175 (2009).
- [51] V. Gavini, S. Baroni, V. Blum, D. R. Bowler, A. Buccheri, J. R. Chelikowsky, S. Das, W. Dawson, P. Delugas, M. Dogan, C. Draxl, G. Galli, L. Genovese, P. Giannozzi, M. Giantomassi, X. Gonze, M. Govoni, F. Gygi, A. Gulans, J. M. Herbert, S. Kokott, T. D. Kühne, K.-H. Liou, T. Miyazaki, P. Motamarri, A. Nakata, J. E. Pask, C. Plessl, L. E. Ratcliff, R. M. Richard, M. Rossi, R. Schade, M. Scheffler, O. Schütt, P. Suryanarayana, M. Torrent, L. Truflandier, T. L. Windus, Q. Xu, V. W.-Z. Yu, and D. Perez, Roadmap on electronic structure codes in the exascale era, *Model. Simul. Mat. Sci. Eng.* **31**, 063301 (2023).
- [52] V. G. Ruiz, W. Liu, E. Zojer, M. Scheffler, and A. Tkatchenko, Density-functional theory with screened van der Waals interactions for the modeling of hybrid inorganic-organic systems, *Phys. Rev. Lett.* **108**, 146103 (2012).
- [53] J. Hermann and A. Tkatchenko, Density functional model for van der Waals interactions: Unifying many-body atomic approaches with nonlocal functionals, *Phys. Rev. Lett.* **124**, 146401 (2020).
- [54] B. Cirera, Y. Litman, C. Lin, A. Akkoush, A. Hammud, M. Wolf, M. Rossi, and T. Kumagai, Charge transfer-mediated dramatic enhancement of Raman scattering upon molecular point contact formation, *Nano Lett.* **22**, 2170 (2022).
- [55] Y. Kunisada and H. Kasai, Hindered rotational physisorption states of H₂ on Ag(111) surfaces, *Phys. Chem. Chem. Phys.* **17**, 19625 (2015).
- [56] V. Kapil, M. Rossi, O. Marsalek, R. Petraglia, Y. Litman, T. Spura, B. Cheng, A. Cuzzocrea, R. H. Meißner, D. M. Wilkins, B. A. Helfrecht, P. Juda, S. P. Bienvenue, W. Fang, J. Kessler, I. Poltavsky, S. Vandenbrande, J. Wieme, C. Corminboeuf, T. D. Kühne, D. E. Manolopoulos, T. E. Markland, J. O. Richardson, A. Tkatchenko, G. A. Tribello, V. V. Speybroeck, and M. Ceriotti, i-PI 2.0: A universal force engine for advanced molecular simulations, *Comput. Phys. Commun.* **236**, 214 (2019).
- [57] C. Schwartz, High-accuracy approximation techniques for analytic functions, *J. Math. Phys.* **26**, 411 (1985).
- [58] D. T. Colbert and W. H. Miller, A novel discrete variable representation for quantum mechanical reactive scattering via the *S*-matrix Kohn method, *J. Chem. Phys.* **96**, 1982 (1992).

- [59] Y. Jiang, S. Pillai, and M. A. Green, Realistic silver optical constants for plasmonics, *Sci. Rep.* **6**, 30605 (2016).
- [60] B. Pettinger, K. F. Domke, D. Zhang, G. Picardi, and R. Schuster, Tip-enhanced Raman scattering: influence of the tip-surface geometry on optical resonance and enhancement, *Surf. Sci.* **603**, 1335 (2009).
- [61] L. Wolniewicz, The $X^1\Sigma_g^+$ state vibration-rotational energies of the H_2 , HD, and D_2 molecules, *J. Chem. Phys.* **78**, 6173 (1983).
- [62] D. K. Veirs and G. M. Rosenblatt, Raman line positions in molecular hydrogen: H_2 , HD, HT, D_2 , DT, and T_2 , *J. Mol. Spectrosc.* **121**, 401 (1987).
- [63] G. K. Teal and G. E. MacWood, The Raman spectra of the isotopic molecules H_2 , HD, and D_2 , *J. Chem. Phys.* **3**, 760 (1935).
- [64] B. N. J. Persson and R. Ryberg, Vibrational line shapes of low-frequency adsorbate modes: CO on Pt(111), *Phys. Rev. B* **40**, 10273 (1989).
- [65] E. W. Smeets and G.-J. Kroes, Designing new SRP density functionals including non-local vdW-DF2 correlation for $H_2 + Cu(111)$ and their transferability to $H_2 + Ag(111)$, $Au(111)$ and $Pt(111)$, *Phys. Chem. Chem. Phys.* **23**, 7875 (2021).
- [66] J. Cui, Y. Zhang, and Z.-C. Dong, Atomistic polarization model for Raman scattering simulations of large metal tips with atomic-scale protrusions at the tip apex, *Nanophotonics* **12**, 4031 (2023).
- [67] R. Kamimura, T. Kondo, K. Motobayashi, and K. Ikeda, Surface-enhanced electronic Raman scattering at various metal surfaces, *Phys. Status Solidi B* **259**, 2100589 (2022).
- [68] T. E. Markland, S. Habershon, and D. E. Manolopoulos, Quantum diffusion of hydrogen and muonium atoms in liquid water and hexagonal ice, *J. Chem. Phys.* **128**, 194506 (2008).
- [69] H. D. Megaw and F. Simon, Density and compressibility of solid hydrogen and deuterium at 4.2 K, *Nature* **138**, 244 (1936).
- [70] Z.-F. Cai, N. Kumar, and R. Zenobi, Probing on-surface chemistry at the nanoscale using tip-enhanced Raman spectroscopy, *CCS Chem.* **5**, 55 (2023).
- [71] J.-L. Yang, Y.-W. Zhou, M.-Y. Jia, Q. Liu, and Z.-F. Cai, Insights into heterogeneous catalysis by tip-enhanced Raman spectroscopy, *ChemCatChem* **16**, e202400370 (2024).

SUPPLEMENTAL MATERIAL: Picocavity-Enhanced Raman Spectroscopy of Physisorbed H₂ and D₂ Molecules

I. METHODS

A. STM-TERS Experiments

The scanning tunneling microscopy (STM) and tip-enhanced Raman spectroscopy (TERS) experiments were performed in an ultrahigh vacuum (UHV) chamber (modified UNISOKU USM-1400) at a sample temperature T of 10 K. A single-crystalline Ag(111) surface (MaTeck) was cleaned by Ar-sputtering-and-annealing cycles in the chamber. H₂ ($\geq 99.999\%$, Westfalen AG) or D₂ (99.7%, Air Liquide) gas was introduced into the STM unit cooled at 10 K via a variable leak valve. The gas exposure (Langmuir; L) is estimated by Pt/n , where P [10^{-6} Torr], t [s], and n denote the displayed pressure value of the gauge (corrected by N₂), the exposure duration, and the correction factor for the gauge, respectively. A Bayard-Alpert ionization gauge is located outside the cryogen-cooled STM unit in the chamber and we used $n = 0.384$ for H₂ and $n = 0.388$ for D₂ [49]. We used a chemically-etched Ag tip that was further sharpened by focused-ion-beam milling as described elsewhere [40]. The bias voltage V_s was applied to the sample while the tip was grounded. The STM images were obtained in the constant current mode at tunneling current I_t of 50 pA. The cleanness of the Ag(111) surface and tip was confirmed by STM images [Fig. S1(a)]. We also confirmed that a TERS spectrum of the Ag–Ag junction before hydrogen dosing had no molecule-derived peaks (Fig. S2, at 0 L).

In the STM junction, p -polarized visible laser (532-nm solid-state or 633-nm HeNe) was directed through a fused silica window and an Ag-coated parabolic mirror. The parabolic mirror is mounted on a five-axis piezoelectric-motor stage in the low-temperature (LT) STM unit and the laser is focused at the tip apex by adjusting the position and angle of the parabolic mirror. The scattered light collected by the parabolic mirror was directed to a spectrometer (AndorShamrock 303i) outside the UHV chamber via a beam splitter and a longpass filter, each selected according to the excitation wavelength λ_{exc} . The nominal incident laser power is 5.9 mW at $\lambda_{\text{exc}} = 532$ nm and 9.7 mW at $\lambda_{\text{exc}} = 633$ nm. For the TERS and STM-induced luminescence (STML) spectra, we used the gratings 150 (for Fig. S10), 600 (Figs. 1, 2, and S2), and 1200 line/mm (Fig. 3 and S11). A lower-density

grating allows the acquisition of spectra over a wider wavelength range, as shown in Fig. S10 (see Sec. II-B), but resulting in broad and asymmetric Raman peaks. Therefore, for the high-frequency-resolution measurements shown in Fig. 3, the densest grating was used.

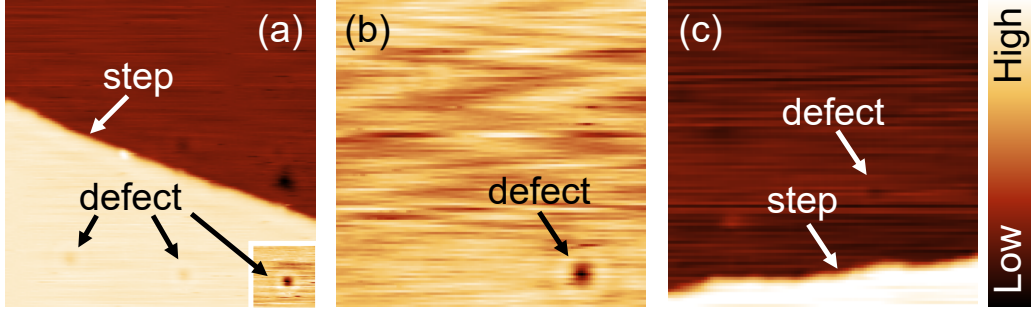


FIG. S1. (a)–(c) Typical STM images of a clean Ag(111) surface, H₂/Ag(111), and D₂/Ag(111), respectively [$V_s = 0.1$ V, $I_t = 0.1$ nA, $T = 10$ K, exposure: H₂ 50 L for (b) and D₂ 220 L for (c), scan size: 40×40 nm² for (a) and (c), 24×24 nm² for (b)]. The inset of (a) shows the STM image of a defect on the clean Ag(111) surface with another color scale. The TERS spectra of H₂/Ag(111) and D₂/Ag(111) shown in Fig. 1b of the main text were obtained with the same sample and tip as (b) and (c), respectively. The circular depressions observed in (b) and (c) are ascribed to subsurface point defects, which also appear on a clean surface as shown in (a) and its inset STM image. Although the appearance of subnanoscale structures such as defects and single Ag atomic steps confirms high spatial resolution imaging, no static hydrogen molecule was observed under the condition used.

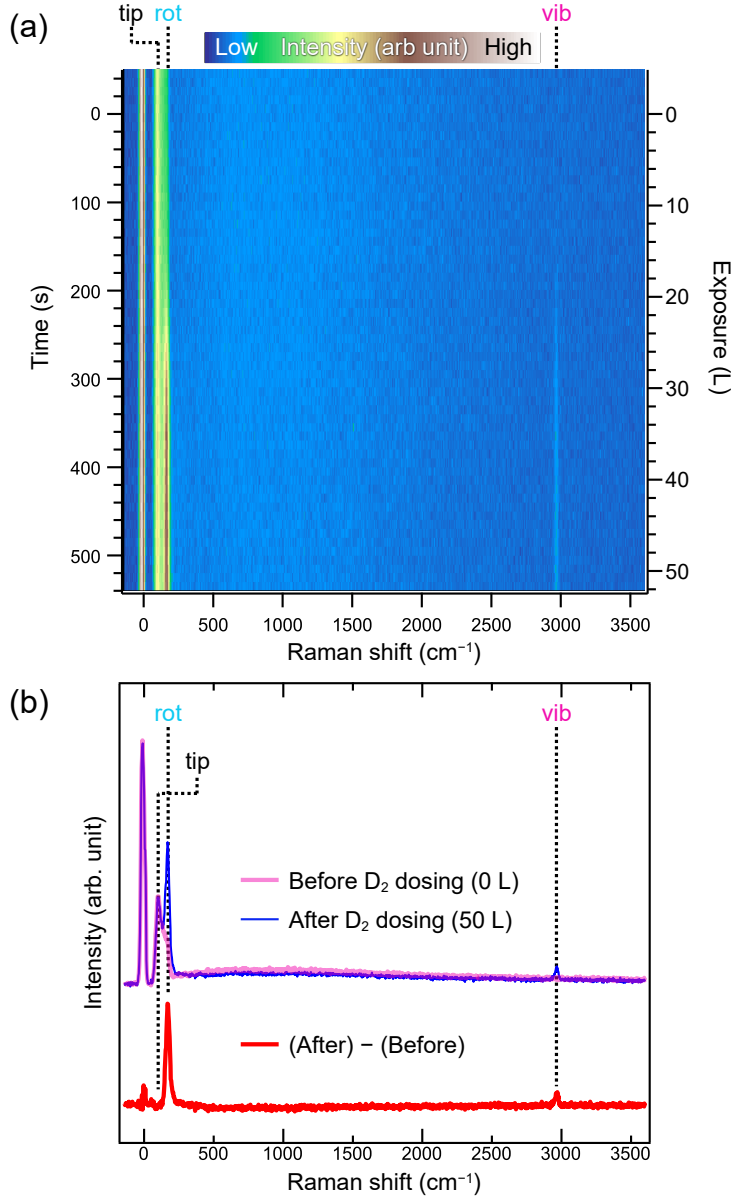


FIG. S2. (a) Waterfall plot of TERS spectra of Ag(111) during D_2 gas exposure ($V_s = 0.01$ V, $I_t = 1$ nA, $T = 10$ K, $\lambda_{\text{exc}} = 532$ nm, accumulation: 10 s/spectrum). The point at which the gas dosing started is set as the origin of the time axis. The “rot” and “vib” modes of *ortho*- D_2 are indicated on top of the plot. The structure at ~ 100 cm^{-1} that was constantly observed before the gas dosing is ascribed to the Ag phonon mode (labeled as “tip”), as described in the main text. (b) TERS spectra of the sample before (bold magenta curve; 0 L) and after (narrow blue curve; 50 L) D_2 gas exposure. The red curve represents the post-dose spectrum subtracted from the pre-dose spectrum, where the “tip” structure is canceled out and only the molecular peaks appear.

B. DFT Calculations and Molecular Dynamics

Density functional theory (DFT) calculations were performed with the FHI-aims program package [50, 51]. We used intermediate defaults for basis sets, radial grids and cutoff potential parameters and light defaults for the Hartree multipole expansion and angular grids. This combination proved efficient and reliable against benchmarks to tight settings. We simulated an orthogonal 4×4 Ag(111) surface cell oriented perpendicular to the z axis, containing four layers. The cell parameters used were $a = 11.554 \text{ \AA}$, $b = 10.007 \text{ \AA}$ and $c = 65.000 \text{ \AA}$. We employed a $2 \times 2 \times 1$ k -point grid and a dipole correction was employed to maximally decouple periodic images along the z direction. We used the Perdew-Burke-Ernzerhof (PBE) exchange-correlation functional and included van der Waals (vdW) interactions through the pairwise screened TS-vdW^{surf} method of Ref. [52] in all simulations reported in the main text. Figure S3 shows a comparison of binding energies with the many-body dispersion correction termed MBD-NL in Ref. [53], indicating a weaker binding energy by only 5 meV and a binding distance 0.1 \AA closer to the surface. Structures were optimized by allowing only hydrogen molecules and the top layer of Ag atoms of the surface to relax. All the other atoms were kept fixed at their bulk (or tip) positions. When we performed simulations including a model tip structure, this was modeled by an Ag₁₉ cluster at varying distances from the surface. The geometry of the tip is shown in Fig. S4. Although this tip size would not be sufficient to capture a proper plasmonic response of the tip, the tip structure can capture the local interactions with molecules close to the tip apex [41, 46, 54].

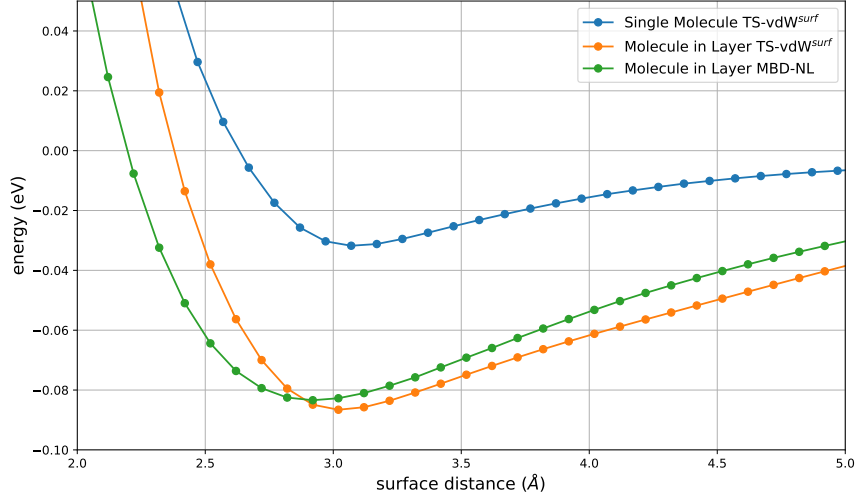


FIG. S3. Binding energies of H_2 to the $\text{Ag}(111)$ surface calculated as the following difference in total energies: $E_b(d_{\text{mol-surf}}) = E_{\text{H}_2/\text{Ag}(111)}(d_{\text{mol-surf}}) - E_{\text{H}_2/\text{Ag}(111)}(10 \text{ \AA})$. In other words, the zero of energy is taken to be the total energy value $E_{\text{H}_2/\text{Ag}(111)}$ when H_2 is 10 \AA away from the surface. The blue curve was calculated with a coverage of $\sim 0.06 \text{ ML}$ (1 molecule per 4×4 surface cell), while the orange and green curves were calculated for a coverage of $\sim 0.69 \text{ ML}$ (11 molecules per surface cell). The PBE functional with $\text{TS-vdW}^{\text{surf}}$ dispersion interactions were used for the blue and orange curves and the PBE functional with the MBD-NL dispersion correction was used for the green curve (see text).

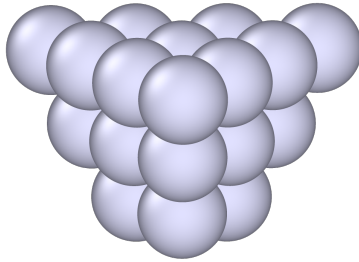


FIG. S4. Geometry used for the model tip structure (Ag_{19} cluster).

We inspected binding sites and binding energies of a single adsorbed H_2 molecule, finding all values in good agreement with previous studies [55]. The binding energy was defined as the difference between the total energy when the molecule was 10 Å away from the surface and the minimum total energy of the adsorbed molecule. The blue curve in Fig. S3 shows the binding curve of a single H_2 molecule adsorbed on the face-centered-cubic (fcc) hollow site of the Ag(111) surface, indicating an equilibrium H_2 –Ag(111) bonding length d_{opt} of 3.09 Å and a binding energy of 32 meV. The model we used in most simulations contained 11 molecules in the unit cell (see rationale below). For this molecular concentration, we evaluated the intermolecular interaction by comparing the binding curves (orange curve in Fig. S3) with that of the single-molecule case (blue); the molecule–molecule interaction in our models amounts to 55 meV/molecule.

Performing vibrational analysis on the optimized single molecule adsorbed on the surface showed that negative frequencies related to rotational and translational modes of the molecule were always present. This led us to consider higher coverages to model local stable clustering of the molecules on the surface. We started by considering a full monolayer (1 ML, i.e., 16 molecules on the 4×4 surface cell), where all fcc-hollow sites of the unit cell were occupied by H_2 . With this setup we performed Born-Oppenheimer molecular dynamics (BOMD) and path-integral molecular dynamics (PIMD) at LT ($T = 20$ K) with the i-PI code [56] connected to FHI-aims. PIMD simulations used 12 beads in conjunction with a normal-mode colored-noise thermostat with 8 auxiliary variables and $\hbar\omega/kT = 500$. This number of beads is not fully converged at this temperature even with the colored-noise quantum thermostats, but the purpose of these simulations was exploratory.

While the full monolayer was stable during more than 10 ps on the classical trajectories, in the quantum trajectory 5 molecules readily desorbed (within the first picosecond) from the substrate, leaving only 11 molecules adsorbed, corresponding to a ~ 0.69 ML coverage. This is the coverage adopted in other simulations in this Letter as the high-density model. For the quantum case, we validated this observation by simulating trajectories with a parameterized Lennard-Jones potential representing the Ag(111) surface. We could calculate the radius of gyration of H atoms from the PIMD simulations, belonging to the 3 molecules closest to the tip at any point in the simulation. For the closest tip distance considered ($d_{\text{tip-surf}} = 7.4$ Å), these were 0.33 Å along x and y and 0.30 Å along z ($T = 20$ K), indicating a small anisotropy. Converting these numbers to an effective thermal de Broglie wavelength Λ and applying a

inverse-square-root scaling for the temperature and mass, we would obtain $\Lambda = 2.3 \text{ \AA}$ for H_2 and 1.5 \AA for D_2 at 10 K. We note that, depending on the density of H_2 molecules on the surface, Λ for H_2 is about the length of the inter-particle spacing at 10 K and signatures of bosonic exchange could begin to be observed. These features are disregarded in the current simulations. Further, we note that even though these simulations provide a clear indication that quantum mechanical effects affect the density of the molecular coverage of the surface, a complete determination would require much longer simulations, which would take years to complete or require the development of a tailored machine-learning potential that surpasses the scope of this work.

Figure S5 shows the energy profiles experienced by an H_2 molecule when varying the distance of its center of mass with respect to the $\text{Ag}(111)$ surface, at different tip-surface distances, and at 0.69 ML coverage. We only varied the position of the molecule closest to the tip apex, while the others were kept at equilibrium. The profile shapes are similar to an asymmetric double-well potential at closer tip-surface distances, while they assume a shape closer to a Morse potential at larger distances, which asymptotically approaches the profile of an H_2 molecule on $\text{Ag}(111)$ without the Ag tip (yellow curve in Fig. S5). The asymmetry of the double-well is strongly impacted by the presence of other molecules on the surface (molecule-molecule interactions). Figure S6(a) shows a comparison with the limiting case of a single molecule in the unit cell (0.06 ML coverage) at a tip-surface distance of 9.4 \AA . In that case (orange curve), if the molecule can overcome the barrier, it will have a higher probability of being found closer to the tip, which was predicted in a Au-tip-single- H_2 -Au-surface junction [17]. As we discuss in the main text, this effect is essential to explain the isotope-dependent redshift observed experimentally.

Figure S6(b) shows a comparison of the 0.69 ML coverage with the tip fixed at $d_{\text{tip-surf}} = 9.4 \text{ \AA}$ and different vdW dispersion corrections, added to the PBE functional. It is clear that details of the vdW dispersion impact the shape of the potential. In this case, the many-body vdW dispersion decreases the distance between the two minima of the asymmetric double-well. This change would impact the quantitative value of the tip-surface distance at which H_2 molecules would prefer to sit closer to the tip, at the low-density limit. We do not expect qualitative changes on the effects we discuss in the main text.

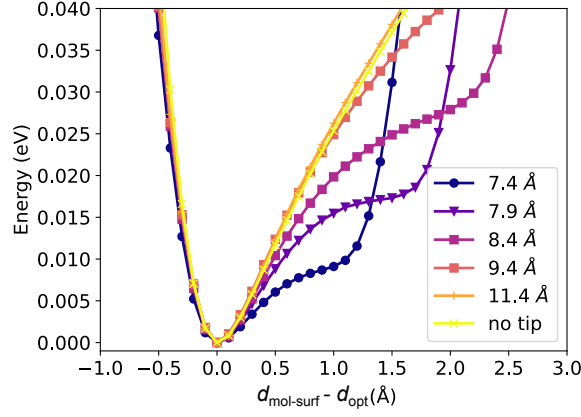


FIG. S5. Energy profiles of an H_2 molecule with varying distance to the $\text{Ag}(111)$ surface without (yellow curve) and with an Ag tip at different tip–surface distances (the other curves). All results obtained with the $\text{PBE}+\text{TS-vdW}^{\text{surf}}$ exchange–correlation functional. For visual clarity, each curve was shifted so that the equilibrium H_2 – $\text{Ag}(111)$ bonding distance and the bonding energy at each tip height is at the origin of the horizontal and vertical axes, respectively.

C. Model 2D Schrödinger Equation

To model the coupling between the intramolecular vibration and the restricted translation of an H_2/D_2 molecule between the substrate and the tip, we constructed a series of two-dimensional (2D) potentials, parametrized by the tip–surface distance $d_{\text{tip-surf}}$,

$$U_{2\text{D}}(d_{\text{mol-surf}}, r_{\text{stretch}}; d_{\text{tip-surf}}) = V(d_{\text{mol-surf}}, d_{\text{tip-surf}}) + \frac{\mu r_{\text{stretch}}^2 \omega^2(d_{\text{mol-surf}}, d_{\text{tip-surf}})}{2}, \quad (\text{S1})$$

where $V(d_{\text{mol-surf}}, d_{\text{tip-surf}})$ is the potential energy of a molecule with its center of mass fixed at a distance $d_{\text{mol-surf}}$ above the substrate surface and with all other coordinates kept at their equilibrium values, as described at the end of Sec. . The vibrational motion along the intramolecular stretching coordinate r_{stretch} is parametrized by the reduced mass μ and angular frequency $\omega(d_{\text{mol-surf}}, d_{\text{tip-surf}})$. We set the mass of a hydrogen atom to $m_{\text{H}} = 1836.1527 m_{\text{e}}$ and use $m_{\text{D}} = 2m_{\text{H}}$, $\mu_{\text{H}_2} = m_{\text{H}}/2$, and $\mu_{\text{D}_2} = m_{\text{D}}/2$, with m_{e} denoting the mass of the electron.

The vibrational frequencies are computed from numerical (finite-difference) second deriva-

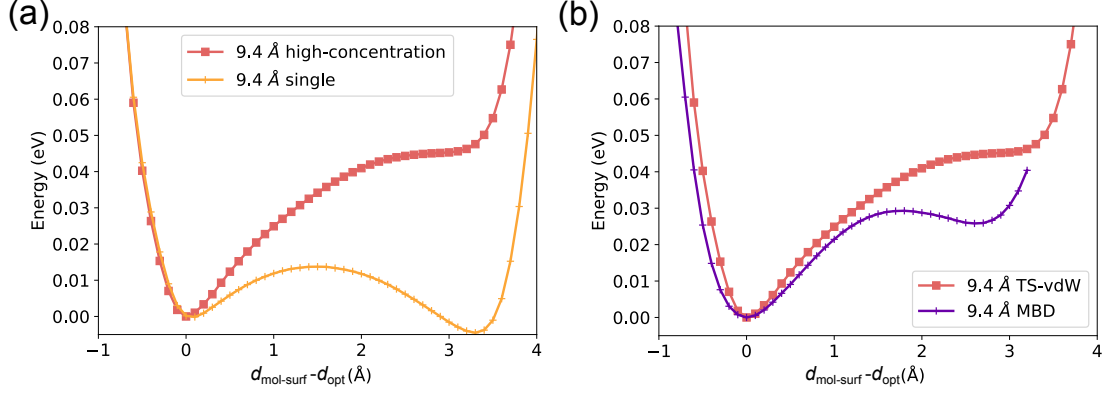


FIG. S6. (a) Energy profiles of an H₂ molecule with varying distance to the Ag(111) surface at a tip-surface distance of 9.4 Å. The red and orange curves indicate the profiles with the higher concentration (11 molecules in the cell) and the lowest concentration (1 molecule in the cell), respectively. The origins of the axes are defined in the same manner as in Fig. S5. (b) Comparison of the high-concentration curve with different vdW corrections (TS-vdW^{surf} [52] and MBD-NL [53]).

tives of the DFT energies with respect to the vibrational coordinate,

$$\omega_{X_2} = \sigma \times \sqrt{\frac{1}{\mu_{X_2}} \frac{\partial^2 V}{\partial r_{\text{stretch}}^2}}, \quad (\text{S2})$$

where $X = \text{H}$ or D and $\sigma = 0.96364$ is a uniform scaling factor that accounts for the difference between the stretch frequency of gas-phase H₂ calculated with our chosen DFT functional and the experimental value. The translational potentials $V(d_{\text{mol-surf}}, d_{\text{tip-surf}})$ and the position-dependent wavenumbers $\nu_{\text{harm}}(d_{\text{mol-surf}}, d_{\text{tip-surf}})$ corresponding to ω_{H_2} are plotted in Fig. S7.

We computed the numerically exact solutions to the 2D Schrödinger equation corresponding to Eq. (S1) using the sinc-function discrete variable representation (DVR) [57, 58]. The equation was solved for high coverage (0.69 ML) with $d_{\text{tip-surf}} = 7.4 \text{ \AA}$ and 9.4 \AA . Given the large separation in the timescales of translational and vibrational motion, we also considered the vibrationally adiabatic approximation, whereby one fixes the translational coordinate $d_{\text{mol-surf}}$ in Eq. (S1) and solves the corresponding one-dimensional (1D) Schrödinger equation in r_{stretch} , with known energy eigenvalues

$$E_{\text{vib},v}(d_{\text{mol-surf}}, d_{\text{tip-surf}}) = \hbar\omega(d_{\text{mol-surf}}, d_{\text{tip-surf}}) \left(v + \frac{1}{2} \right), \quad (\text{S3})$$

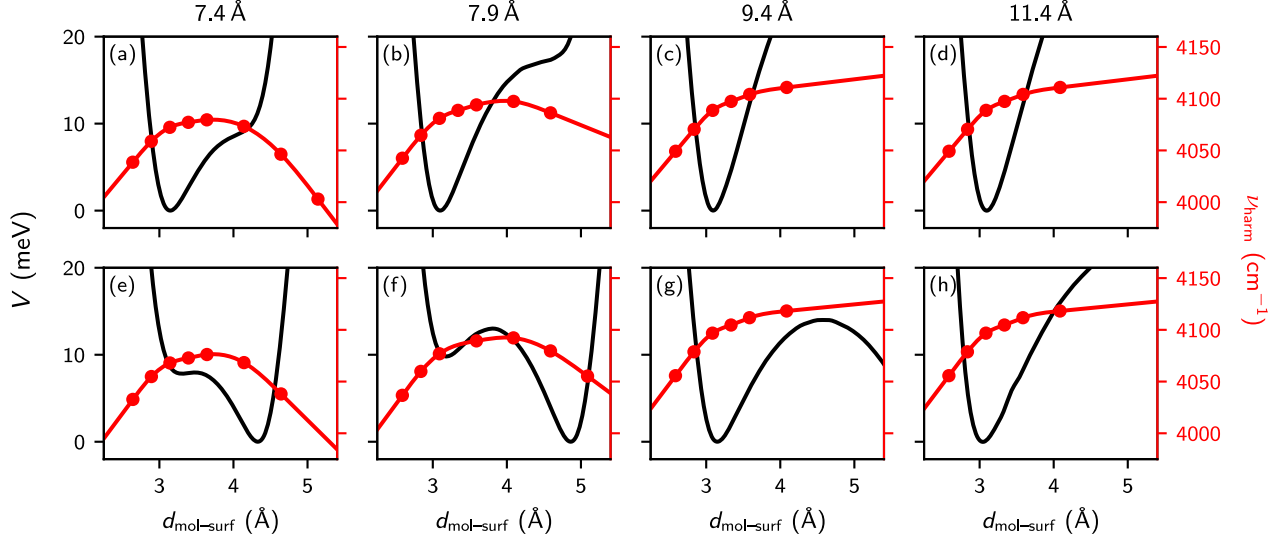


FIG. S7. Translational potential energy profiles $V(d_{\text{mol-surf}}, d_{\text{tip-surf}})$ and H_2 vibrational wavenumbers $\nu_{\text{harm}}(d_{\text{mol-surf}}, d_{\text{tip-surf}})$ corresponding to the frequencies in Eq. (S2), shown with black and red lines, respectively. Panels (a–d) show the parameters for 0.69 ML coverage, and panels (e–h) show the parameters for 0.06 ML coverage. The headings above the panels show the values of $d_{\text{tip-surf}}$. The translational energies were computed on a dense grid, whereas the frequencies were calculated at a select few points, shown with red circles. We use cubic spline interpolation to construct smooth curves and linear extrapolation to extend the curves beyond the grid boundaries. Values of ν_{harm} at $d_{\text{tip-surf}} = 11.4 \text{ \AA}$ are copied over from $d_{\text{tip-surf}} = 9.4 \text{ \AA}$, since point calculations confirm that harmonic stretch frequencies are essentially independent of $d_{\text{tip-surf}}$ over the relevant range of $d_{\text{mol-surf}}$ at these tip-surface separations.

where \hbar is the reduced Planck constant and $v = 0, 1, 2, \dots$ is the vibrational quantum number. These are then used to construct the vibrationally adiabatic translational potential,

$$U_{1\text{D},v}(d_{\text{mol-surf}}; d_{\text{tip-surf}}) = V(d_{\text{mol-surf}}, d_{\text{tip-surf}}) + E_{\text{vib},v}(d_{\text{mol-surf}}, d_{\text{tip-surf}}), \quad (\text{S4})$$

for which we solve the 1D Schrödinger equation numerically using DVR. The energy difference between the ground state solutions for $v = 0$ and 1 is an excellent approximation to the vibrational excitation energy of the 2D model (see Table S1). Given the accuracy of the vibrationally adiabatic approximation, we adopt it in all subsequent calculations.

In Tables S2 and S3, we give the vibrational transition energies computed for the H_2 and D_2 molecules at high and low coverages. For illustration purposes (see Fig. 4 in the

main text), we have also computed the zero-point energies (ZPEs) and mean molecular displacements for the bare translational potentials $V(d_{\text{mol-surf}}, d_{\text{tip-surf}})$. From the computed values of ν , it is apparent that if both H_2 and D_2 present a similar coverage, our model cannot explain the anomalous isotope effect observed experimentally. However, if H_2 exhibits a low coverage and D_2 exhibits a high coverage, the experimental trends are well accounted for [see also Fig. 4(e) in the main text]. However, it is challenging to determine the local molecular concentration near the tip apex at any measurement, and a deeper study of the vibrational frequency variation could provide indirect hints to the concentrations observed in experiment. Although we neglected the anharmonic character of the H–H stretching coordinate, this effect should not change the qualitative discussion and will only introduce uniform redshifts in the values reported here.

TABLE S1. Vibrational excitation energies calculated from the numerical solutions of the Schrödinger equations corresponding to the 2D model in Eq. (S1) and the vibrationally adiabatic 1D model in Eq. (S4). The top row indicates the values of $d_{\text{tip-surf}}$. The number of significant figures in the 2D solutions was estimated by varying the grid step and bounds in the DVR. The 1D solutions are converged to at least the number of significant figures shown below.

| | 7.4 (Å) | | 9.4 (Å) | |
|----|--|--|--|--|
| | ν_{H_2} (cm ⁻¹) | ν_{D_2} (cm ⁻¹) | ν_{H_2} (cm ⁻¹) | ν_{D_2} (cm ⁻¹) |
| 2D | 4073.69 | 2880.45 | 4089.44 | 2891.58 |
| 1D | 4073.685 | 2880.452 | 4089.442 | 2891.582 |

D. TERS Spectrum Simulation

We conducted TERS simulations according to the methodology proposed in Refs. [46]. We used Tip A discussed in Ref. [54] and calculated the anharmonic Raman spectrum based on an *ab initio* molecular dynamics (AIMD) trajectory (5 ps) of a molecular layer adsorbed on the surface and a tip apex located 4 Å above the molecular layer at $T = 20$ K. We calculated the TERS intensity as $I^{\text{TERS}} \propto \int dt e^{i\omega t} \langle \alpha_{zz}^{\text{local}}(0) \alpha_{zz}^{\text{local}}(t) \rangle$, where $\alpha_{zz}^{\text{local}}$ was obtained by a local polarizability calculation at each geometry in the time-series given by the molecular dynamics. For this part of the calculation, we only considered the free-standing molecular

TABLE S2. ZPEs, mean molecule–surface displacements ($\langle d_{\text{tip-surf}} \rangle$) and vibrational transition frequencies (ν) computed for H_2 at high (0.69 ML) and low (0.06 ML) coverages, corresponding to the top and bottom rows of Fig. S7, respectively. The ZPE and $\langle d_{\text{tip-surf}} \rangle$ are computed by solving the 1D Schrödinger equation for *only* the translational potential, $V(d_{\text{mol-surf}}, d_{\text{tip-surf}})$. The ZPE shown here is reported for the lowest-energy state localized in the well marked in Figs. 4(b) for the high coverage and 4(d) for the low coverage. The vibrational transition frequencies are computed for the 2D model within the vibrationally adiabatic approximation. The low-coverage data are used for plotting the bullets and the vertical lines on them in Fig. 4(d) and “ H_2 calc” in Fig. 4(e) of the main text. The low-coverage values are used for comparison with the experimental plots in Fig. 4(e).

| $d_{\text{tip-surf}}$ (Å) | 0.69 ML | | | 0.06 ML | | |
|---------------------------|-----------|---|----------------------------|-----------|---|----------------------------|
| | ZPE (meV) | $\langle d_{\text{mol-surf}} \rangle$ (Å) | ν (cm^{-1}) | ZPE (meV) | $\langle d_{\text{mol-surf}} \rangle$ (Å) | ν (cm^{-1}) |
| 11.4 | 9.7 | 3.22 | 4089.57 | 8.0 | 3.25 | 4097.62 |
| 9.4 | 9.8 | 3.22 | 4089.44 | 7.5 | 3.37 | 4101.79 |
| 7.9 | 8.5 | 3.28 | 4083.09 | 7.9 | 4.66 | 4071.55 |
| 7.4 | 7.0 | 3.41 | 4073.68 | 6.8 | 4.06 | 4063.34 |

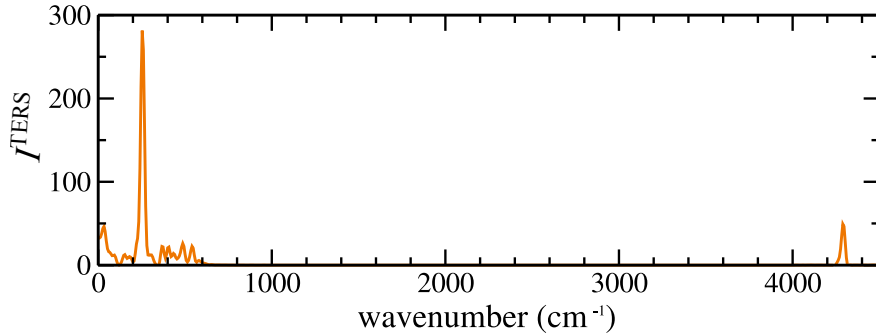


FIG. S8. Simulated anharmonic TERS spectrum of H_2 in a tip–surface junction.

layer (no surface) at the positions adopted in the AIMD trajectory including the surface. We note that the method of Ref. [46] is unable to capture the plasmonic enhancement in its totality. We do not observe any noteworthy features in the calculated spectrum and it overall agrees with the experimental spectrum. The redshift of the rotational band in the simulation is explained by the absence of nuclear spin in the simulations, making calculations

TABLE S3. Same as Table S2 but for D₂. In this case, the high-coverage (0.69 ML) data are used for plotting the bullets and the vertical lines on them in Fig. 4(b) and “D₂ calc” in Fig. 4(e) of the main text.

| $d_{\text{tip-surf}}$ (Å) | 0.69 ML | | | 0.06 ML | | |
|---------------------------|-----------|---|---------------------------|-----------|---|---------------------------|
| | ZPE (meV) | $\langle d_{\text{mol-surf}} \rangle$ (Å) | ν (cm ⁻¹) | ZPE (meV) | $\langle d_{\text{mol-surf}} \rangle$ (Å) | ν (cm ⁻¹) |
| 11.4 | 7.1 | 3.18 | 2891.66 | 5.9 | 3.19 | 2896.83 |
| 9.4 | 7.2 | 3.18 | 2891.58 | 5.7 | 3.30 | 2899.92 |
| 7.9 | 6.3 | 3.22 | 2886.81 | 6.0 | 4.74 | 2878.13 |
| 7.4 | 5.3 | 3.33 | 2880.45 | 5.2 | 4.15 | 2872.51 |

reproduce only classical rotations. These are incapable of capturing the quantization of the rotational transitions and thus do not capture the $J = 0 \rightarrow 2$ transition of *para*-H₂, where J is the rotational quantum number. This explains the redshift observed in the simulated frequency of this transition with respect to the experimental value. This simulation is of exploratory character, as achieving statistical convergence through the use of parametrized machine-learned potentials along with accurate plasmonic enhancements is beyond the scope of this paper.

E. FEM Simulations

To evaluate the electric field in the STM junction, we performed finite element method (FEM) simulations using COMSOL Multiphysics (version 6.2 with the Wave Optics Module). We used the three-dimensional model with an Ag tip and Ag sample plate in a vacuum [40]. The tip shaft is elongated in z direction with a half opening angle of 6° from a 30-nm radius sphere [Fig. S9(a)]. The tip is axisymmetrical to z [see the inset of Fig. 2(c) for the xyz coordinate] with a length of 300 nm. To reproduce a plasmonic picocavity in the STM junction, at the apex of the Ag tip, an Ag half sphere with a radius of 0.5 nm is attached as an atomic-scale protrusion [Fig. S9(b)]. For comparison [the orange dotted curve in Fig. 2(c) of the main text], we also constructed another Ag tip model with an effective radius of 30 nm without the atomic-scale protrusion. A p -polarized plane wave with $\lambda_{\text{exc}} = 532$ nm and an electric field $|E_0|$ of 1 V/m is incident with an angle of 55° relative to the z axis. The

perfectly matched layers surrounding the volume are set to absorb all outgoing waves. The dielectric constant of the Ag objects is referenced from the literature [59]. The z component of the electric field E_z is sampled.

An Ag flat plate with a thickness of 100 nm is placed beneath the tip apex with a gap distance d_{FEM} , as shown in [Fig. S9(b)]. As shown in Table S3, the molecular height $d_{\text{mol-surf}}$ is calculated to be 0.32–0.33 nm for D₂/Ag(111) [Fig. S9(c)]. In the d_{FEM} definition, taking into account the atomic radius of Ag, the position of the molecule corresponds to ~ 0.2 nm above the Ag surface plane in the FEM model [the open bullet in Fig. S9(b)]. Although the calculated $d_{\text{mol-surf}}$ depends on the tip height (Table S3), the FEM model used the constant height for the sampling point at any d_{FEM} . We confirmed that differences in the molecular position on the order of 0.1 nm do not result in qualitative differences in the $|E_z|$ curve shape. To directly compare with the experimental TERS intensities, the electric field enhancement factor $(|E_z|/|E_0|)^4$ (Ref. [60]) is displayed in Fig. 2(c). To the field enhancement of the nearest neighboring molecule, assuming the molecule is placed in the next adsorption site of Ag(111), $x = 0.29$ nm is used [red triangle in the inset of Fig. 2(c)]. Thus, when the point at the surface just under the tip is defined as $(x, y, z) = (0, 0, 0)$, the black and red curves shown in Fig. 2c of the main text represent the plots sampling at $(x, y, z) = (0, 0, 0.20)$ nm and $(0.29, 0, 0.20)$ nm, respectively.

As shown in Fig. 2, the gap distances with the FEM simulations $d_{\text{FEM}} = 550$ pm to 850 pm well reproduced the Raman enhancement at the experimental tip height $z_{\text{exp}} = -300$ to 0 pm. Considering the Ag-atom radius, $d_{\text{tip-surf}}$ for the simulations (Fig. 4 in the main text) is comparable to $d_{\text{FEM}} + 0.3$ nm [Fig. S9(b) and (c)]. Therefore, $z_{\text{exp}} = -300$ pm corresponds to $d_{\text{tip-surf}} \approx 0.8$ nm, which was used for the alignment of the experimental and theoretical plots of the vibrational frequency shifts $\Delta\nu$ [Fig. 4(e)].

II. SUPPLEMENTAL RESULTS AND DISCUSSION

A. Nuclear Spin Isomers

H₂ and D₂ have two nuclear spin isomers, *ortho* and *para*. *para*-H₂ (nuclear spin quantum number $I = 0$) is more stable than *ortho*-H₂ ($I = 1$) by 14 meV [61]. *para*-H₂ has only even J , whereas *ortho*-H₂ has only odd J . Although *ortho*-H₂ is the predominant species

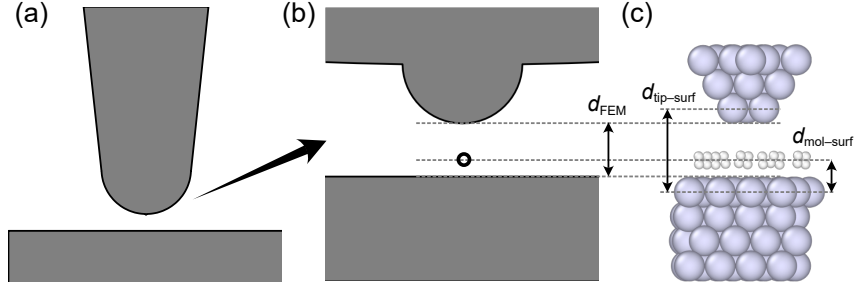


FIG. S9. Side-view schemes for FEM. (a) Wide-area view for the FEM simulation. Gray objects correspond to Ag. Note that the 0.5-nm radius protrusion at the tip apex is too small to be visible. (b) Magnified view of the junction. Black open bullet indicates the sampling position of the electric field [see the black curve of Fig. 2(c) in the main text]. (c) Side-view of the DFT model [Fig.4(a) in the main text] in the same scale as the FEM model in (b) for the comparison.

in the gas phase at room temperature (a temperature equilibrium composition of 75%), the molecular adsorption on metals enhances the *ortho*-to-*para* conversion, leading to the dominance of the *para* species on the surfaces [4]. In the TERS spectra, we can detect only *para*-H₂ (Table S4); as a reference, in the gas phase, *ortho*-H₂ have a Raman-active rotational mode [$(\nu, J) = (0, 1) \rightarrow (0, 3)$] at $\sim 587 \text{ cm}^{-1}$ [61, 62]. This implies that we detected only the physisorbed species after *ortho-para* conversion on the surface. In the case of D₂, *ortho* ($I = 0, 2$) is more stable than *para* ($I = 1$) by 7.4 meV and more dominant (67%) in the gas phase at room temperature. Only *ortho*-D₂ was detected in our TERS spectra, indicating again that *para*-D₂ was converted on the surface.

Although we introduced normal hydrogen gases (*n*-H₂ and *n*-D₂) into the chamber, we observed rotational/vibrational transitions only for *para*-H₂ and *ortho*-D₂ in the TERS spectra (Fig. 1 in the main text). The dominance of *para*-H₂ on Ag(111) in the TERS spectra ($T = 10 \text{ K}$) is consistent with a previous study with high-resolution electron energy loss spectroscopy (HREELS) for H₂ on an Ag film (exposures of 0.5–10 L, $T = 10 \text{ K}$) [8], whereas some previous reports detect *ortho*-H₂ on Ag(111). A HREELS study on H₂/Ag(111) at 6 K [11] shows that rotational mode peaks of both *para*-H₂ and *ortho*-H₂ were detected under a higher H₂ pressure ($9.0 \times 10^{-8} \text{ Torr}$) while *para*-H₂ was dominantly detected under a lower pressure ($2.0 \times 10^{-9} \text{ Torr}$). Photostimulated desorption studies [14, 15] shows that at an exposure of 30 L and a temperature of $\sim 6 \text{ K}$, *ortho*-H₂ and *para*-D₂ are alive on Ag(111) on

the order of hundred seconds and that the conversion of D_2 is slower than H_2 .

To compare with the above-mentioned studies, we performed TERS measurements while exposing D_2 to a clean Ag(111) surfaces, as shown in Fig. S2. The gas pressure was set to 9.7×10^{-8} Torr, comparable with the EELS study [11]. The *ortho*- D_2 -derived peaks appeared at ~ 16 L and then saturated at ~ 40 L, while *para*- D_2 was not detected. The weak intensity at low exposures may be due to molecular diffusion along the surface at low coverages and the weak contribution of neighboring molecules to the TERS signal [see Fig. 2(c) in the main text]. It should be noted that even if the gas pressure and exposure values are comparable, the molecular coverage varies depending on the chamber configuration. Nevertheless, we confirmed that *ortho*- H_2 and *para*- D_2 were not detected at any pressures and exposures we used ($0.8\text{--}2 \times 10^{-7}$ Torr; $10^2\text{--}10^3$ L). The HREELS observation of the metastable isomer at 6 K only at high exposures [11] may be attributed to be hydrogen multilayers, where the second layer does not interact with the Ag surface. For our LT-TERS measurement, in contrast, only a monolayer would be formed at the higher temperature, 10 K. Another possibility that the metastable isomer were not detected in TERS is that the localized surface plasmonic resonance (LSPR) in the gap is accelerating the *para*-to-*ortho* conversion of the molecule under the tip. Although far-field 532-nm irradiation did not affect the conversion rate [15], the strong electric field localized in the STM junction could interact with the nuclear spin of the adsorbate.

B. Excitation Wavelength Dependence

To verify the contribution of LSPR to the TERS intensity, we examined the excitation wavelength (λ_{exc}) dependence. Figure S10(a) shows a STML spectrum recorded over a clean Ag(111) surface with an Ag tip. The LSPR results in a broad spectral feature in the visible range with a maximum at ~ 560 nm. After recording the STML, we exposed the surface to the D_2 gas, conducting TERS measurements with $\lambda_{\text{exc}} = 532$ and 633 nm [Figs. S10(b) and S10(c), respectively]. The peak intensity of each mode significantly changes with λ_{exc} , whereas the Raman shift value is unchanged. The vibrational intensity is weakened with $\lambda_{\text{exc}} = 633$ nm, indicating the corresponding Raman scattering is not efficiently enhanced by the LSPR because the peak position (a wavelength of the Raman scattering λ_{Raman} of 779 nm) is located in the weak resonance range of the LSPR [Fig. S10(a)]. In contrast, both

TABLE S4. Frequencies of rotation/vibrotation modes of molecular hydrogen detected experimentally (in cm^{-1}). From the TERS results in this study, data from a wide-frequency-range spectra [“low res.”; Fig. 1(a) in the main text] and from spectra with higher energy resolution [“high res.”; Figs. 3(a)–3(d)] are displayed. Since the vibration frequency of $\text{H}_2/\text{Ag}(111)$ is largely redshifted by the tip proximity, the values at a far tip distance [a relative tip height of -110 pm in Figs. 3(a)–3(d)] are shown as the high resolution data.

| System | On Ag(111) | | On Ag film | On Cu(001) | Gas phase | |
|--------------|-----------------|------------------|---------------------|---------------------|--------------------|--------------------|
| Method | TERS (low res.) | TERS (high res.) | HREELS ^a | HREELS ^b | Raman ^c | Raman ^d |
| H_2 | | | | | | |
| rot | 351 | 348 | 395 | 363 | 354.5 | 354.365 |
| vib | 4121 | 4134 | 4178 | 4178 | - | 4161.200 |
| rot+vib | 4443 | - | 4533 | 4517 | - | 4497.848 |
| D_2 | | | | | | |
| rot | 169 | 172 | - | 177 | 178.8 | 179.108 |
| vib | 2967 | 2968 | - | 3000 | 2996.1 | 2993.6 |
| rot+vib | 3133 | - | - | 3170 | 3166.3 | - |

^a Ref. [8].

^b Ref. [9].

^c Ref. [63].

^d Ref. [62].

the rotational and vibrational peaks become intense with $\lambda_{\text{exc}} = 532$ nm because they are more resonant with the LSPR.

C. Tip-Height Dependence of Peak Intensity and Width

To obtain the waterfall plots shown in Fig. 3 of the main text, we conducted tip approach-and-retraction procedures while recording the TERS spectra [41, 54]. Figure S11(a) is the full dataset for the H_2 “vib” mode shown in Fig. 3(b) of the main text. During recording TERS spectra, the tip height was lowered stepwise and then the tip was retracted from the surface. The symmetrical waterfall plot with respect to the closest tip height indicates the non-destructive measurement in the tip approach-and-retraction process. Figure S11(b)

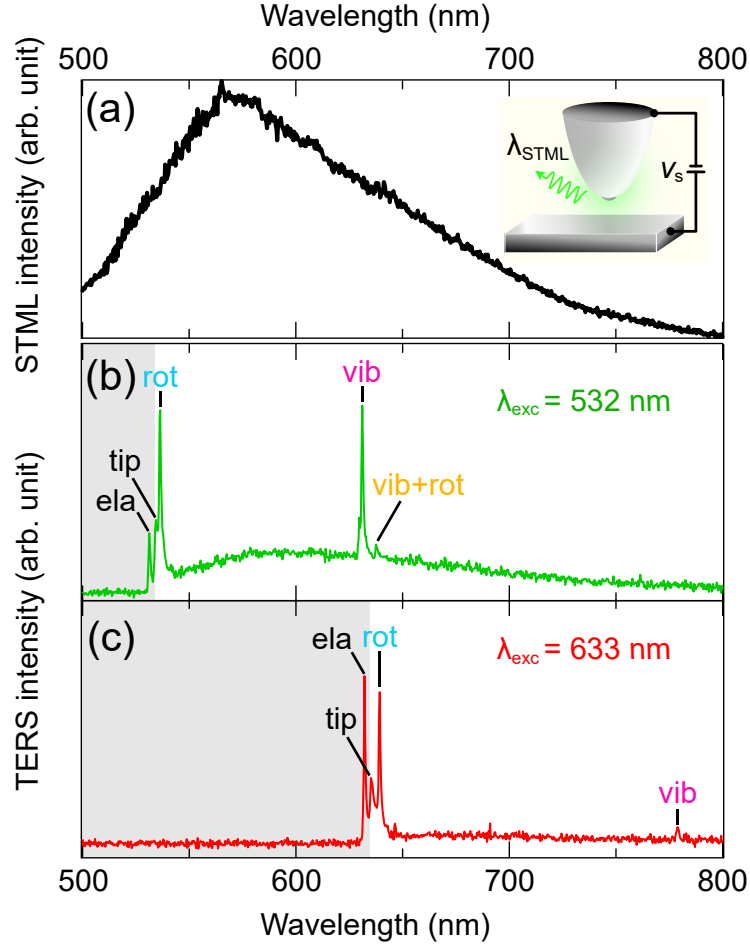


FIG. S10. Correlation between Raman scattering and plasmonic resonance in the STM junction. (a) STML recorded over a clean Ag(111) surface with an Ag tip ($V_s = 3$ V, $I_t = 5$ nA, $T = 10$ K). The inset shows the schematic of the STML experiment. The horizontal axis is the luminescence wavelength λ_{STML} . After recording this spectrum, the surface was exposed to the D_2 gas. (b and c) TERS spectra of $\text{D}_2/\text{Ag}(111)$ with $\lambda_{\text{exc}} = 532$ and 633 nm, respectively ($V_s = 10$ mV, $I_t = 1$ nA), using the Ag tip as in (a). The horizontal axis is indicated by wavelength λ_{Raman} instead of the Raman shift. The gray background represents the long-pass filtered region. “ela” represents the peak of the elastic (i.e., Rayleigh) scattering with its intensity suppressed by the filter.

shows the horizontal line profiles of the waterfall plot for the H_2 “vib” mode at the points indicated by the arrows in the same color. The three spectra indicates the redshift and broadening of the H_2 “vib” peak as the gap distance decreases.

During recording the waterfall TERS plot, we occasionally observed a sudden intensity

change caused presumably by the modification of the tip apex structure due to the strong tip-surface interaction at the small gap. Figure S11(c) shows an example, where a sudden drop of the TERS intensity was observed. The modification of the plasmon background intensity implies that the atomic-scale structure was changed by the strong attractive force exerted when the tip was brought close to the surface. At the same time as the plasmon feature, the D₂ “rot” peak was also dropped, while the frequency of the “rot” mode is unchanged. This observation is in good agreement with the enhancement mechanism described in the main text (Fig. 2); the picocavity-derived electric field plays a crucial role in the TERS intensity of physisorbed hydrogen molecules.

To determine the experimental peak position shift $\Delta\nu$ as a function of the tip height z_{exp} in Fig. 4(e) of the main text, the line profile of the waterfall plots at each tip height [Fig. 3 in the main text; see also Fig. S11(b)] was fitted by a Gaussian peak with a constant background. The top and bottom panels of Fig. S12 shows the peak position and width, respectively, as a function of the tip height for the rotational (a) and vibrational (b) modes. To display the experimental peak-shift values $\Delta\nu(z_{\text{exp}}) = \nu(z_{\text{exp}}) - \nu(z_{\text{ref}})$, the reference point z_{ref} should be specified. Ideally z_{ref} is the furthest tip height at which the peak was detected. However, since using a too weak peak as the reference value $\nu(z_{\text{ref}})$ causes large errors in the $\Delta\nu(z_{\text{exp}})$ plot, we adopted as z_{ref} the tip height at which the error value below 2 cm^{-1} based on the peak fitting. The error bars in Fig. S12 indicate the standard deviation of the fitting. As the tip approaches, the peak intensity increases, reducing the error. As shown in the arrows in Fig. S12, we set $z_{\text{ref}} = -90, -80, -90, -50$ pm for H₂ rot, D₂ rot, H₂ vib, and D₂ vib, respectively, determining the origin of each peak shift. For the H₂ and D₂ “vib” modes [top panel of Fig. S12(b)], the $\Delta\nu$ plots at $z_{\text{exp}} \leq z_{\text{ref}}$ were used as the experimental curves shown in Fig. 4(e) of the main text. In Fig. 4(e) of the main text, the experimental tip height $z_{\text{exp}} = -280$ pm is aligned to the tip-sample distance $d_{\text{tip-surf}} = 0.74$ nm for the calculations. Although the accurate determination of the experimental tip-sample gap distance is difficult, this alignment is reasonable; as described in Sec. I-E, $z_{\text{exp}} = -300$ pm is comparable with $d_{\text{FEM}} = 550$ pm and $d_{\text{tip-surf}} \approx 0.8$ nm.

As shown in Fig. S12(a), the frequency and width of the H₂ and D₂ “rot” peaks are almost unchanged by the tip. In contrast, the bottom panel Fig. S12(b) shows the strong peak broadening for the H₂ “vib” mode [see also Fig. S11(b)] whereas the peak width for D₂ “vib” is almost unchanged. A possible origin of the peak broadening is the anharmonicity,

which can modify the lifetime of molecular vibrations [64]. It is also entirely possible that if neighboring molecules influence the experimental signal [see Fig. 2(c) in the main text], they would lead to the high-frequency shoulder of the vibration transition for H_2 , as these molecules would still lie on the surface [Fig. 3(c)] and would therefore present a higher ν than the ones on the tip, which instead provide the most enhanced signal; however, this effect may not be pronounced because the coverage of H_2 is less than that of D_2 (see Sec. I-C). Another possible origin is the movement of the molecule in the junction; because the double-well potential barrier is very small [see Fig. 4(d) in the main text], the H_2 molecule near the tip apex can move to a metastable site near the surface or adjacent adsorption sites on the surface [18] by a small voltage bias or plasmonic field applied in the STM junction. This movement instantaneously occurring during the acquisition time of the Raman spectrum can also modify the peak shape of the vibrational mode. We expect that the coexistence of these factors leads to the characteristic peak width depending on the tip height.

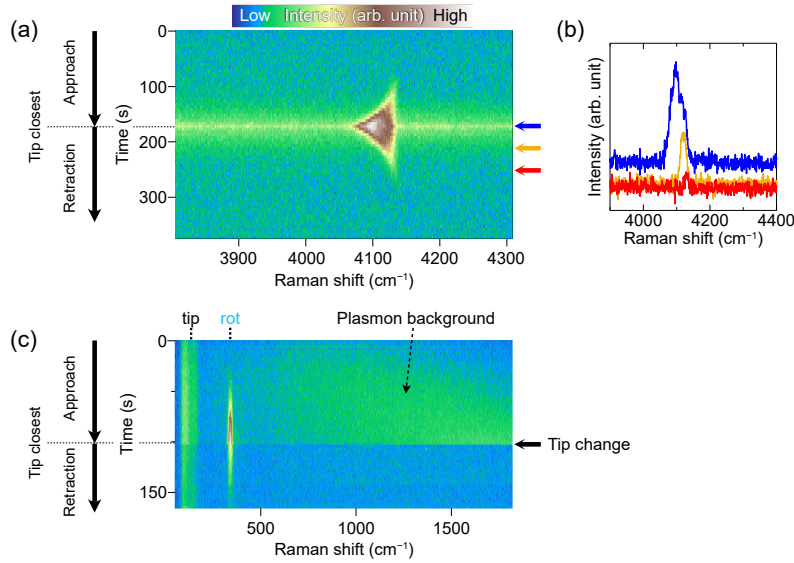


FIG. S11. (a) Full-scale waterfall plot of the high-resolution TERS spectrum for the H_2 “vib” mode shown in Fig. 3(b) of the main text. (b) TERS spectra of $\text{H}_2/\text{Ag}(111)$, corresponding to the horizontal line profiles in (a) indicated by the arrows in the same color. No vertical offset is applied to the graph; the blue spectrum has a higher constant background as shown in (a). (c) Waterfall plot of the high-resolution TERS spectrum for the H_2 “rot” mode, where a sudden drop of the TERS intensity was observed.

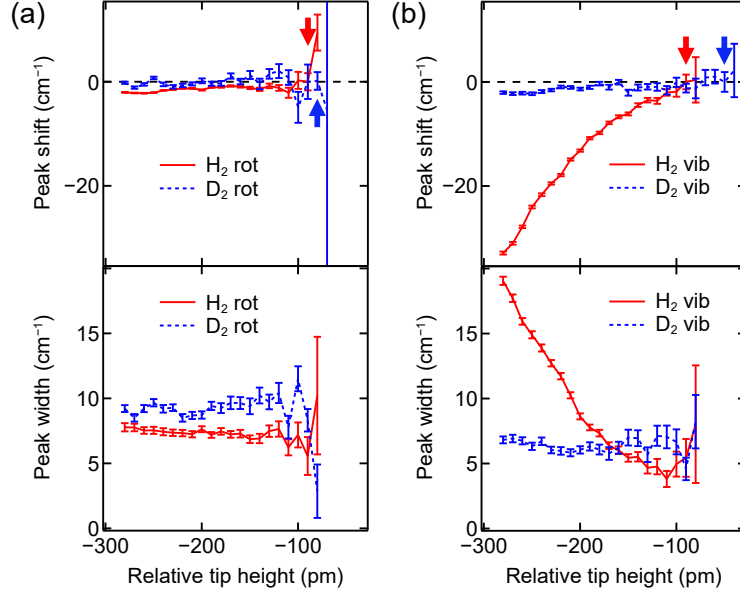


FIG. S12. (a) Tip-height dependence of the peak position (top panel) and the full width at half maximum (bottom panel) for H₂ “rot” (red curve) and D₂ “rot” (blue curve). The error bars indicate the standard deviation of the fitting. (b) Same as in (a) but for H₂ “vib” (red curve) and D₂ “vib” (blue curve) by the fitting of the spectra shown in Fig. 3(c) and (d) in the main text, respectively. The arrows indicate the reference points with the errors below 2 cm⁻¹.